

## Three-dimensional fingering structures in immiscible flow at the crossover from viscous to capillary fingering

Anindityo Patmonoaji\*, Moshlih Muharrik, Yingxue Hu, Chunwei Zhang, Tetsuya Suekane

Department of Mechanical Engineering, Tokyo Institute of Technology, 2-12-1-16-33, Ookayama, Meguro-ku, Tokyo, 152-8550, Japan



### ARTICLE INFO

#### Article history:

Received 22 May 2019

Revised 15 October 2019

Accepted 21 October 2019

Available online 22 October 2019

#### Keywords:

Microtomography

Displacement

Capillary fingering

Viscous fingering

Crossover

Pore-throat

### ABSTRACT

Fluid displacement experiments were performed with immiscible fluids in a packed bed of glass spheres. The three-dimensional (3D) structure of the fingering pattern was visualized by computer tomography (CT) for a range of capillary numbers ( $Ca$ ) between  $5.22 \times 10^{-7}$  and  $1.04 \times 10^{-4}$  at the viscosity ratio of  $\log M = -2.203$  in the absence of the influence of buoyancy force. Based on the 3D CT images, the characteristics of the fingering pattern at the crossover from viscous fingering (VF) to capillary fingering (CF) were investigated quantitatively. The structure of the fingering pattern changed gradually from streak-like for VF to more compact for CF with a decrease in  $Ca$ . Associated with the crossover from VF to CF, saturation of the invading phase (IP) and the fractal number of the structure both increased. The invaded pore size and invaded throat size distributions were also estimated for all values of  $Ca$ . The invaded pore size distribution was similar for all  $Ca$  values, but a clear shift in the throat size distribution was observed with the crossover from VF to CF.

© 2019 Elsevier Ltd. All rights reserved.

### 1. Introduction

The displacement process of one fluid by another in porous media has been observed in various fields such as hydrocarbon resource recovery, groundwater contamination, and carbon capture and storage (CCS). The rate of oil recovery by self-production owing to internal reservoir pressure is as low as 10–25% of the original oil in place (OOIP) because of a sharp decrease in pressure (Lashkarbolooki et al., 2016a,b). The most widely used approach to maintaining reservoir pressure is injection of water into the oil reservoir. However, in secondary recovery, the recovered petroleum is only about 25–45% of OOIP after the primary recovery stage (Lashkarbolooki et al., 2016a,b). In addition, more than half of the petroleum cannot be recovered owing to instability at the interface of immiscible fluid pairs such as water-oil and gas-oil. For groundwater, contamination by non-aqueous phase liquids (NAPLs) has been remediated with pump-and-treat schemes, in which fresh water is injected into the contaminated groundwater to displace the NAPL. However, again owing to instability at the interface of immiscible fluid pairs, some portion of the NAPL remains in the groundwater (Mackay and Cherry, 1989). In the application of CCS, the instability at the interface of immiscible fluid pairs also reduces the efficiency of the process (Suekane and Okada, 2013). As

$CO_2$  is injected into deep saline aquifers, which are saturated with brine, this instability reduces the displacement of the brine, decreasing effective utilization of the full storage capacity.

For the displacement processes between immiscible fluid pairs in porous media, two types of fingering, i.e., capillary fingering (CF) and viscous fingering (VF) have been widely observed under the negligible buoyancy effect. The fingering regimes are well described by the  $\log Ca$ - $\log M$  diagram, where  $Ca$  corresponds to capillary number and  $M$  corresponds to viscosity ratio, as first introduced by Lenormand et al. (1988). When a less viscous fluid displaces a more viscous fluid ( $\log M < 0$ ), a condition that is sometimes referred as *unfavorable*, VF occurs over a wide range of  $Ca$  values, depending on stabilization by interfacial tension (Homsky, 1987; Lashkarbolooki et al., 2016a; Løvoll et al., 2005; Saffman, 1986). At low flow rates, CF dominates over VF. At infinitesimally low flow rates, a condition that can be modeled by invasion percolation theory (Wilkinson and Willemse, 1983), the invading phase (IP) selectively penetrates the surrounding pores filled with the defending phase (DP), depending on pore size. A non-wetting phase injected into the wetting phase of a saturated porous medium, a process that is often referred to as *drainage*, selectively invades the biggest pore among the surrounding pores because the capillary entrance pressure that must be overcome to enter the pore is the smallest. On the other hand, for injection of a wetting phase into a non-wetting phase saturated porous medium, i.e., an *imbibition* process, the smallest pore throat is spontaneously invaded because it exhibits the highest suction

\* Corresponding author.

E-mail address: [patmonoaji.aaa@m.titech.ac.jp](mailto:patmonoaji.aaa@m.titech.ac.jp) (A. Patmonoaji).

capillary pressure. Later, we discuss transition of the invaded pore size associated with the crossover from VF to CF in the imbibition process.

For the sake of visualization, the majority of past experimental work has been performed in a Hele-Shaw cell or a two-dimension (2D) porous medium. Wang et al. (2013) studied transition from CF to VF in a 2D micromodel using a scCO<sub>2</sub>-water pair ( $\log M = -1.25$ ) and found that transition occurred at  $\log Ca = -5.91$ , corresponding to  $Ca = 1.23 \times 10^{-6}$ . Using the same 2D micromodel, Zhang et al. (2011) conducted a series of experiments using seven non-wetting and wetting fluids with  $\log M$  ranging from -1.95 to 1.88; they found that the crossover shifted to low  $Ca$  with a decrease in  $\log M$ . Islam et al. (2014) observed the transition from CF to VF in a vertical 2D Hele-Shaw cell with an air-water pair ( $\log M = -1.73$ ) to simulate displacement and fracture during leakage. Using an analytical model, Holtzman and Juanes (2010) investigated the crossover between VF and CF in a deformable 2D porous medium with pore-scale disorder. However, reports of 3D experimental work remain scarce owing to the difficulties of displacement observations inside opaque 3D porous media. The main reports of 3D displacement works were mainly numerical simulation (Dias and Wilkinson, 1986; Tsuji et al., 2016; Wilkinson, 1984) results instead of experimental observation.

The recent development of X-ray micro tomography has advanced the study of multiphase flow from 2D to 3D porous media (Muhsarrik et al., 2018; Nakanishi et al., 2016; Patmonoaji et al., 2018; Patmonoaji and Suekane, 2017; Suekane et al., 2015; Wang et al., 2016). By utilizing micro-CT, we investigated the characteristics of VF, CF, and the crossover between them in a 3D porous medium during an imbibition process, in which the wetting phase was used as the IP to displace the non-wetting phase as the DP saturating the porous medium. Based on the pore-scale resolved images, various properties of the fingering patterns, i.e., saturation, number of fingers, pore-throat occupation by the IP, and fractal dimension, are also discussed. To the best of our knowledge, this is the first study to visualize VF, CF, and their crossover in 3D porous media.

## 2. Experimental methods

### 2.1. Experimental setup

To observe the flow structure inside the porous medium, a micro-CT scanner, Comscantechno Co., Scan Xmate-RB 090 SS, was utilized. Scanning was performed under a dynamic mode, where the scanned object remained still while an X-ray source and a detector rotated around the sample to perform the scan; thus avoiding drift in the position of the scanned object in the image space. Each scan was performed for about 90 s by scanning the sample 1000 times through 360-degrees in all directions. The same X-ray power (90 kV and 90  $\mu$ A) was used throughout the experiments to provide identical brightness and contrast. A series of cross-sectional images of the porous medium with a uniform voxel size of 16.262  $\mu$ m was obtained. Ultimately, a 3D image with a resolution of 992  $\times$  992  $\times$  992 voxels (16.13  $\times$  16.13  $\times$  16.13 mm<sup>3</sup>) was obtained.

The porous medium was assembled by packing glass beads into an acrylic cylindrical container with an internal diameter of 10 mm. One of the main problems with a packed bed used as a porous medium is preferential flow through the high porosity layer against the wall (wall effect) (Roozbahani et al., 2012). To address this problem, a radial layer of a combination of water-wet glass beads of diameter 400  $\mu$ m (As One, BZ-01, 350–500  $\mu$ m) and oil-wet glass beads of 100  $\mu$ m (As One, BZ-01, 105–125  $\mu$ m) was used. The oil-wet glass beads were obtained directly from the manufacturer and were surface-stained with oil, rendering them weakly

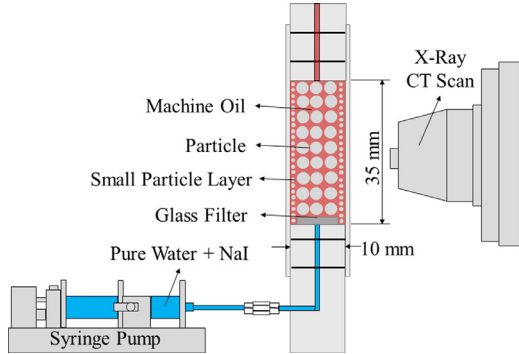


**Fig. 1.** Schematic of experimental setup.

oil-wet. The water-wet glass beads were produced by washing the glass beads with toluene, ethanol, and water, consecutively, to remove the oil stain. Glass beads of 400- $\mu$ m diameter were placed the center of the container, whereas glass beads of 100- $\mu$ m diameter were placed near the container wall. This radial layer formation was generated using a hollow cylinder. Before packing, the hollow cylinder was placed into the center of the container and the 100- $\mu$ m diameter glass beads poured into the region outside of the hollow cylinder. Afterward, the 400- $\mu$ m diameter glass beads were poured into the hollow cylinder. All of the particles were poured into the container gradually while shaking the container to generate a close, randomly packed, porous medium, as classified by Dullien (1992). After the height of the particles reached  $35 \pm 0.5$  mm, the hollow cylinder was removed to form the layers. As a result, the 100- $\mu$ m glass beads occupied the region near the wall with a thickness of  $0.5 \pm 0.1$  mm. With this radial structure of different sizes and wettabilities, the porosity near the wall was reduced and smaller pore-throat preferential fluid intrusion in the CF regime during imbibition was prevented.

In addition, to remove the effects of point injection, low permeability filters made of sintered glass were placed at the injection location. After these packing procedures, the properties of the porous medium were measured. Permeability was measured using a water flooding test, giving a result of  $1.36 \pm 0.054 \times 10^{-10}$  m<sup>2</sup>. Porosity ( $\phi$ ), pore size distribution, and throat size distribution were measured by processing of the X-ray images, which will be discussed in the next section. The porosity was  $0.38 \pm 0.02$ , whereas the median pore diameter ( $d_{p, 50}$ ) and median throat diameter ( $d_{t, 50}$ ) were 206  $\mu$ m and 132  $\mu$ m, respectively. The experimental schematic showing the porous medium is shown in Fig. 1.

For the fluid pair, machine oil (Shin-Etsu Chemical Co., Ltd., HIVAC-F-5) and water doped with 10 wt% sodium iodide (NaI) were used as the DP and IP, respectively. The water was doped with NaI, which has a high X-ray attenuation coefficient, to enhance its contrast among the other phases. Because the glass beads were mainly water-wet, water was the wetting phase, whereas oil was the non-wetting phase. The density ( $\rho$ ) of both liquids was measured using a gravimetric method, with both liquids showing a similar density. Consequently, the displacement processes were only affected by competition between capillary and viscous forces. The viscosity ( $\mu$ ) of the oil was taken from the information provided by the supplier, whereas the viscosity of the water was measured with a falling ball viscometer (Thermo Scientific HAAKE Type C). Interfacial tension ( $\sigma$ ) between the fluids was measured via a pendant drop technique using an interfacial tension meter (Kruss, DAS25S). All experiments were conducted under room conditions (0.1 MPa and  $298 \pm 2$  K). Viscosity ratio ( $M$ ) was also calculated based on the following equation:

$$M = \frac{\mu_i}{\mu_d} \quad (1)$$

**Table 1**  
Physical properties of fluids.

Fluids	Viscosity (mPas)	Density (kg/m <sup>3</sup> )	Interfacial tension (mN/m)	Log of viscosity ratio
Machine oil	175.5	1096	34.3	-2.203
Water (10% NaI)	1.012	1097		

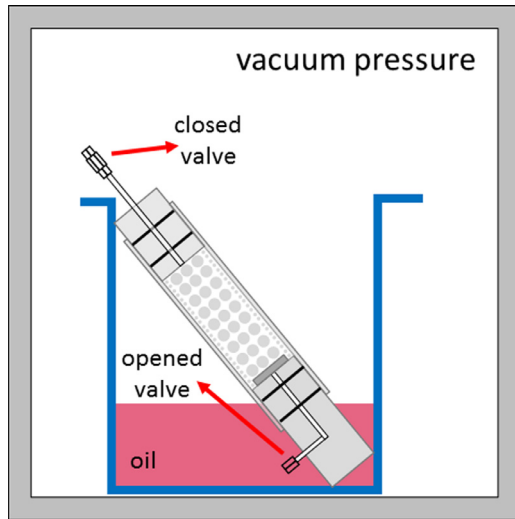


**Fig. 2.** Schematic procedure to fully saturate the porous medium with oil.

where subscripts *i* and *d* denote the IP and the DP, respectively. The measured and calculated properties of these fluids are given in Table 1.

## 2.2. Experimental procedures

To saturate the porous medium with machine oil, it was partly submerged in an oil-filled container inside a vacuum chamber as given in Fig. 2. The top outlet of the porous medium was closed, whereas the bottom inlet was opened. By vacuuming the chamber for about an hour, the air inside the porous medium escapes as bubbles in the pool of machine oil, leaving it in a vacuum state. As the pressure in the vacuum chamber brought back to atmospheric pressure, the incoming air forced the oil into the porous medium promptly, yielding perfect saturation without air bubbles.

Next, the porous medium was placed into the micro-CT and water imbibition was performed at a constant injection flow rate that was controlled by a syringe pump (KD Scientific, IC3100). The non-dimensional capillary number (*Ca*) and Reynolds number (*Re*) were defined as

$$Ca = \frac{\mu_i u_i}{\sigma} \quad (2)$$

$$Re = \frac{\rho_i u_i d_{50}}{\mu_i} \quad (3)$$

where *u* is Darcy velocity and *d*<sub>50</sub> is median particle diameter. *Ca* was used as a parameter to compare the viscous and the capillary forces that affect the flow regime. Because the experiment was performed at a constant unfavorable viscosity ratio (*M* < 1) and negligible buoyancy, the flow regime should have been affected by *Ca* only. As demonstrated by Lenormand et al. (1988) and Zhang et al. (2011), the flow regimes of VF, CF, and the crossover of VF–CF can be observed by controlling *Ca* under these conditions. *Re* was used as a monitoring parameter to check that the experiment was conducted under a Darcy regime (*Re* < 10). The highest *Re* in these experiments was 1.299. The experimental flow rates

and other parameters are given in Table 2. In the present study, we did not take images during the evolution of fingering because the CT scan could not keep pace with the relatively fast injection speed. Therefore, only the images taken at breakthrough, which was defined as the condition when the IP reached the outlet, were scanned after stopping the injection.

## 3. Image processing method

To obtain qualitative as well as quantitative data of the displacement process, image processing techniques were applied. The workflow of the image processing techniques is illustrated in Fig. 3.

A sample cross-sectional image is given in Fig. 3a. The region of interest (ROI) in our observation was defined as the area filled by the glass beads of 400 μm. Hence, the area near the wall, i.e., that filled with glass beads of 100 μm, was excluded. This area corresponds to a diameter of about 9 mm. In addition, owing to the limitations of the cone-beam scan of the micro-CT, the images near the top and the bottom of the scan (corresponding to about 1-mm height each) were excluded from the processing. As a result, the ROI of the observation was a cylindrical volume with a diameter of ~9 mm and height of ~13 mm.

At first, the characteristics of the porous medium were investigated by separating the solid from the fluids in the cross-sectional CT images. Prior to binarization, noise was removed by applying a median filter. Direct thresholding of image gray values was then used to binarize the image. A 3D representation of this binarized image is shown in Fig. 3b. With these binarized images, the porosity at every cross section was evaluated based on the fraction of pore area relative to total area. Afterward, pores and throats were identified via a watershed-segmentation method by implementing a plug-in of the ImageJ software (3D ImageJ Suite) (Ollion et al., 2013). This method separated the pores and throats by using the information in a distance map, which was calculated using Euclidean distance (Danielsson, 1980). Pores were detected as volumetric objects and throats were detected as the planes separating two pores. The equivalent diameter was then used to characterize the size of the pores and throats. The final 3D image of a segmented pore-throat is given in Fig. 3c.

Direct thresholding was also applied to the CT images of the IP at breakthrough. A 3D image of the IP is shown in Fig. 3d. Noise removal was performed by applying object detection via a 3D object counter plug-in (Bolte and Cordelieres, 2006) to remove clusters smaller than 1000 voxels. Based on the binarized images of the IP at breakthrough, various parameters were estimated, as follows. First, the saturation of the IP was evaluated in each cross section as the fraction of the area of IP relative to the area of the pore. Second, to estimate the number of fingers, the 3D structure of the IP was divided into slab sections (thickness of 50 slices) in the flow direction, as shown in Fig. 3e. The number of separated IP clusters in each slab was counted using an ImageJ plug-in (3D object counter) (Bolte and Cordelieres, 2006). Third, the 3D structure of the IP (Fig. 3d) was compared with the locations of pores and throats (Fig. 3c). If the center of the pore or throat was detected inside the IP, the pore or throat was regarded to have been invaded by the IP. Fourth, the fractal dimension of the 3D structure of the IP was estimated using a 3D box counting method, as illustrated in Fig. 3f. The 3D structure of the displacing fluid was separated based on the size of box *s*. Every box was then checked

**Table 2**  
Imbibition parameters.

Flow rate (mL/min)	Darcy velocity (m/day)	Capillary number (-)	Reynolds number (-)
16.608	304.55	$1.04 \times 10^{-4}$	1.299
8.336	152.86	$5.22 \times 10^{-5}$	$6.521 \times 10^{-1}$
0.834	15.29	$5.22 \times 10^{-6}$	$6.522 \times 10^{-2}$
0.626	11.48	$3.92 \times 10^{-6}$	$4.897 \times 10^{-2}$
0.417	7.64	$2.61 \times 10^{-6}$	$3.259 \times 10^{-2}$
0.209	3.84	$1.31 \times 10^{-6}$	$1.638 \times 10^{-2}$
0.083	1.53	$5.22 \times 10^{-7}$	$6.527 \times 10^{-3}$

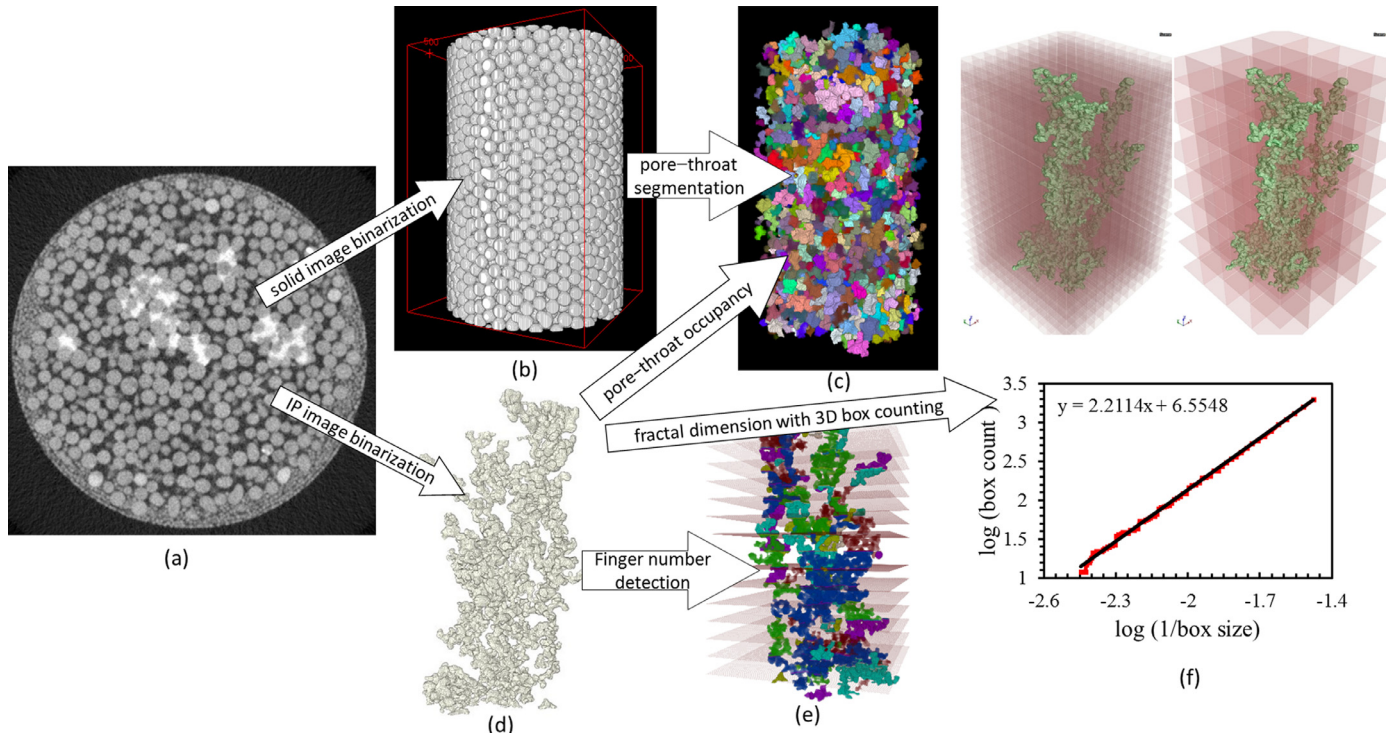


**Fig. 3.** Workflow of the image processing schemes (a) X-ray cross-sectional image with bright as the IP, dark as the DP, and gray as the solid; (b) binarized image of the solid; (c) segmented pore–throat with different colors indicating a separated pore–throat; (d) binarized image of the IP; (e) number of fingers measured in each slab of 50 slices (on average), with different colors indicating different fingers; and (f) fractal dimension measurements with the box counting method. (For interpretation of the references to color in this figure legend, the reader is referred to the web version of this article.)

to determine whether it contained the displacing fluid. The data for the number of boxes that contained the displacing fluid  $N(s)$  and the length of boxes  $1/s$  were used to calculate the fractal dimension; the estimated slope of  $\log N(s) - \log 1/s$  is the fractal dimension value. Fifth, the surface area of the IP was determined by measuring the perimeter of the voxelized IP in each cross section. This perimeter was then multiplied by the voxel height to obtain the surface area in each cross section. The total 3D surface area of the IP was calculated by summing all of the surface areas calculated in each cross section.

## 4. Results and discussion

### 4.1. Displacement structure visualization at breakthrough

The 3D structure of the IP at breakthrough is visualized in Fig. 4 for all values of  $Ca$ . As demonstrated throughout Fig. 4a–g, the displacement structures tend to be more compact as  $Ca$  decreases (Chen et al., 2017; Islam et al., 2014; Lenormand et al., 1988; Wang et al., 2013; Zhang et al., 2011). At high  $Ca$  values ( $1.04 \times 10^{-4}$ ,  $5.22 \times 10^{-5}$ , and  $5.22 \times 10^{-6}$ ) the flow patterns demonstrated a forward-progressing pattern with several branches, resembling a streak-like structure, which is a characteristic of

VF. At high  $Ca$  values, the viscous force became dominant over the capillary force and a pressure gradient was established in the mean flow direction. Once the displacement front deformed because of VF, the IP flowed faster owing to the low viscosity (as compared with the DF for same pressure gradient). As a result, the IP preferentially extended with a streak-like structure (Lenormand et al., 1988). Among these three flow structures, the fingers at  $Ca = 5.22 \times 10^{-6}$  (Fig. 4c) were thicker and more concentrated. The sparse fingers at  $Ca$  of  $1.04 \times 10^{-4}$  and  $5.22 \times 10^{-5}$  were typically the size of a few pores; however, the thicker fingers at  $Ca = 5.22 \times 10^{-6}$  were larger than a few pores. Further, as  $Ca$  decreased, this streak-like structure diminished and a more compact structure emerged (Fig. 4d–g). This gradual change in structure demonstrates the VF–CF crossover. With a decrease in  $Ca$ , the pressure in each phase tended to be constant and uniform because of the negligible pressure gradient by the viscous shear force. Therefore, the IP tended to invade the smallest throats among the neighboring pores filled with DF. As a result, the IP extended in various directions, even the backward direction, as shown by the red circles in Fig. 4d–f. By further lowering  $Ca$ , the viscous force became less dominant and the capillary force became more significant. At the lowest  $Ca$  ( $5.22 \times 10^{-7}$ ), a much more compact structure was generated (Fig. 4g).

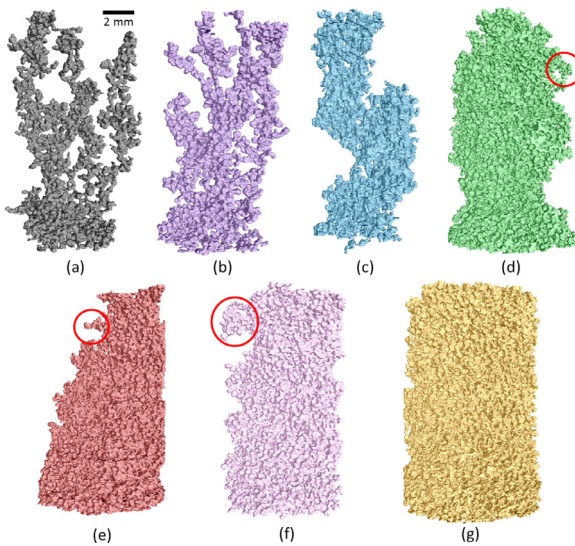


**Fig. 4.** Change in 3D structure of the IP at breakthrough for  $\text{Ca}$  values of (a)  $1.04 \times 10^{-4}$ , (b)  $5.22 \times 10^{-5}$ , (c)  $5.22 \times 10^{-6}$ , (d)  $3.92 \times 10^{-6}$ , (e)  $2.61 \times 10^{-6}$ , (f)  $1.31 \times 10^{-6}$ , and (g)  $5.22 \times 10^{-7}$ . Branches denoted in red circles extend horizontally (or opposite to the mean flow direction), reflecting the properties of CF. (For interpretation of the references to color in this figure legend, the reader is referred to the web version of this article.)

**Fig. 5a** shows the distribution of trapped DP clusters at  $\text{Ca} = 5.22 \times 10^{-7}$ , corresponding to the IF of **Fig. 4g**. There were a large number of small trapped IP clusters of single pore size; there also existed large clusters spreading over several to tens of pores. The size distribution of the trapped DP clusters is given in **Fig. 5b** as a log-log scale graph of normalized frequency ( $N(s)$ ) for a given class of cluster size ( $s$ ). As described by percolation theory (Dias and Wilkinson, 1986),  $N(s)$  at a given class of  $s$  follows a power law relation that is usually expressed as

$$N(s) \sim s^{-\tau} \quad (4)$$

where  $\tau$  is a constant. By analyzing the trapped cluster distribution with this scheme, we found that  $\tau$  was between 1.0 and 1.2. This value is in agreement with the analysis of Iglaue and Wülling (2016) and indicates that the displacement process resembles an invasion percolation process (Dias and Wilkinson, 1986).

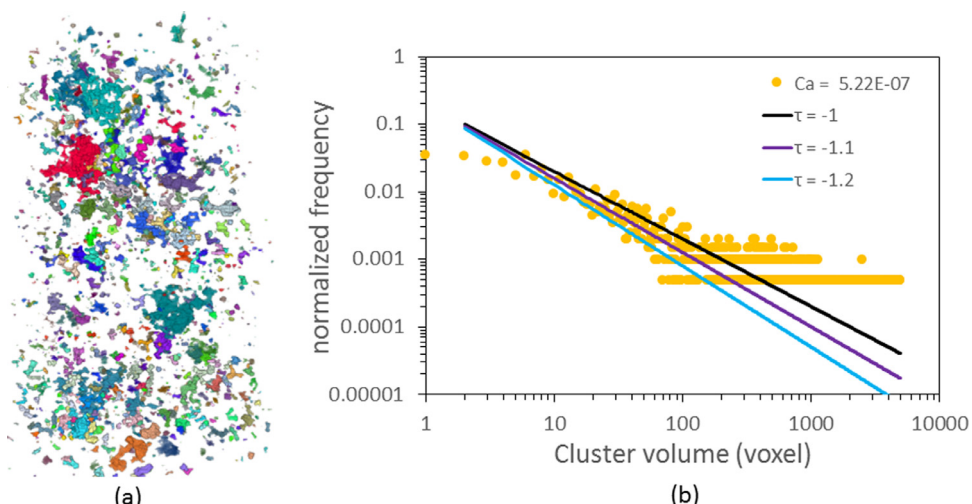
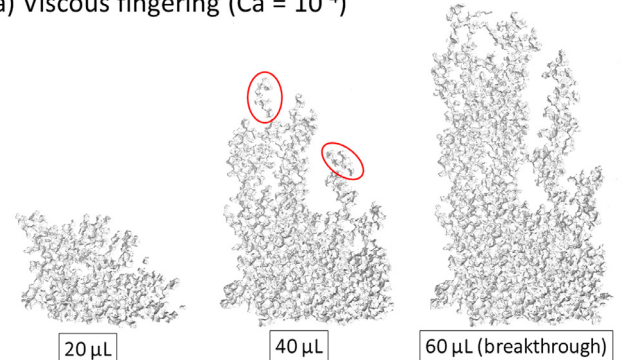


**Fig. 5.** (a) Distribution of trapped DP clusters at  $\text{Ca} = 5.22 \times 10^{-7}$ , corresponding to the IF of **Fig. 3g**. Separate clusters are labeled by coloring. (b) Cluster size frequency versus cluster size. (For interpretation of the references to color in this figure legend, the reader is referred to the web version of this article.)

(a) Viscous fingering ( $\text{Ca} = 10^{-4}$ )



(b) Capillary fingering ( $\text{Ca} = 10^{-7}$ )

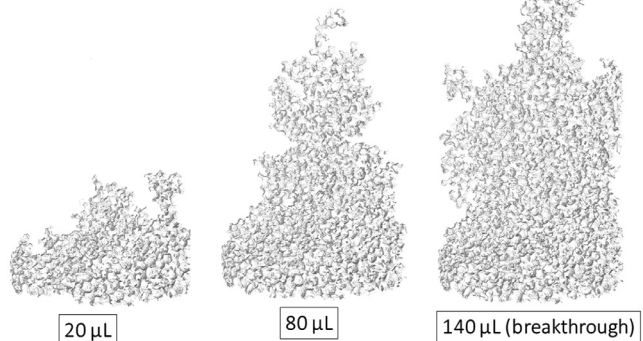


**Fig. 6.** Step by step injection and scanning of displacement process for (a) VF and (b) CF. The red circles mark the detached IP due to fluid rearrangement when the injection was stopped. (For interpretation of the references to color in this figure legend, the reader is referred to the web version of this article.)

#### 4.2. Displacement structure visualization prior to breakthrough

As supplementaries, we conducted additional observations for the displacement structure prior to breakthrough. This was performed by injecting the IP step by step at much lower amount than the breakthrough accompanied with subsequent scanning of micro-CT. Two additional experiments were performed with the same viscosity ratio at capillary number of  $10^{-4}$  and  $10^{-7}$  as representations of VF and CF, respectively. Those observations are given in **Fig. 6a** and b for VF and CF, respectively. From the **Fig. 6a** for

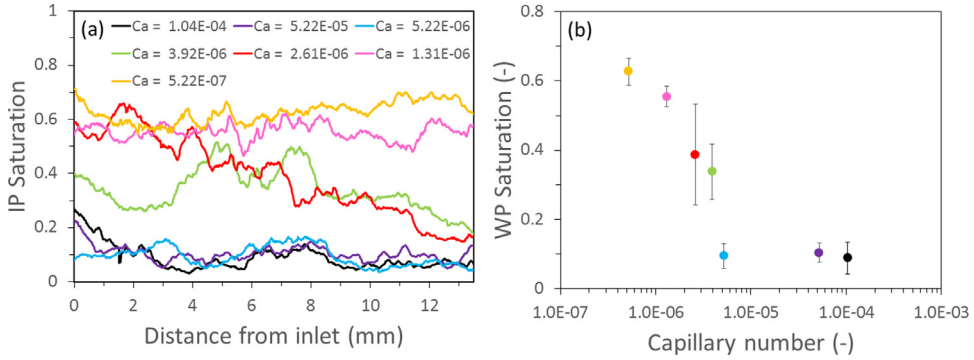


**Fig. 7.** (a) Cross-sectional (local) average of IP saturation along the packed bed and (b) the total (global) average of IP saturation versus  $\text{Ca}$  (error bars show standard deviation).

VF, it was clear that the development of viscous fingering occurs by forming streak-like structures. These streak-like structures then kept progressing to the outlet direction. From the Fig. 6b for CF, the displacement structure did not proceed only to outlet direction but also to radial direction and even inlet direction, which is the main feature of CF. As shown in the right most images in Fig. 6a and 6b, which represents the breakthrough image from step by step injection, the image more or less shows the same structure with the breakthrough image in Fig. 4, which correspond to breakthrough image from continuous injection. However, as marked by the red circle in Fig. 6a, the IP was detached from the main displacement structure, which occurs due to fluid rearrangement (Garing et al., 2017). When the injection was stopped, and the scanned was performed, the fluid rearrangement could occur. Although the breakthrough images of the step by step injection and continuous injection were more or less the same, we are afraid that this step by step injection will further affect the finger phenomena during further injection due to the fluid rearrangement, especially for high VF. In VF, the pressure distribution is not stable due to the rapid movement of the fluid. As a result, fluid rearrangement could occur easier. Therefore, to make a consistent experiment design, all of the observations were performed at breakthrough condition under continuous injection. In addition, previous reports of displacement characteristics were performed at breakthrough conditions under continuous injection (Holtzman and Juanes, 2010; Islam et al., 2014; Lenormand et al., 1988).

Another characteristics of displacement in porous media is a Haines jump (Armstrong et al., 2015; Berg et al., 2013; Zacharoudiou et al., 2018). To catch the Haines jump phenomena in 3D, however, high performance microtomography method such as used by Berg et al. (2013) was required to catch the event. In our work, we could not catch the Haines jump phenomena because of the limitation in our microtomography. The Haines jump that occurs in this experiment mainly has become untraceable because they have merged with the generated finger. Nevertheless, our focus is not related with the temporal evolution of the finger, but to the whole final condition of the finger after the displacement.

#### 4.3. Local and global saturation of IP

The cross-sectional average (local) distribution of saturation of the IP along the porous medium sample, together with the whole (global) average saturation for all experiments, are given in Fig. 7a and b, respectively. For high  $\text{Ca}$  values ( $1.04 \times 10^{-4}$ ,  $5.22 \times 10^{-5}$ , and  $5.22 \times 10^{-6}$ ), the local saturation remained low (0.031–0.267) across the porous medium. The global saturation was also low, in the range of 0.088–0.104. This low saturation reflects the VF with its streak-like structure, as discussed above and as observed by

other researchers (Chen et al., 2017; Islam et al., 2014; Lenormand et al., 1988; Wang et al., 2013; Zhang et al., 2011). However, as the  $\text{Ca}$  decreased below  $5.22 \times 10^{-6}$ , the global saturation increased gradually, demonstrating a crossover from VF to CF. As the flow became more capillary-controlled, the invasion progress of the forward-progressing pattern started to diminish and extended in all directions, generating more saturation. From the local saturation at  $\text{Ca} = 3.92 \times 10^{-6}$ , the local saturation fluctuated in the range of 0.148–0.517, whereas  $\text{Ca} = 2.61 \times 10^{-6}$  generated a high level of saturation near the inlet (about 0.65), gradually decreasing to 0.16. This decreasing saturation along the mean flow direction at the crossover from VF to CF may reflect competition between VF and CF at breakthrough. With a decrease in  $\text{Ca}$ , the global saturation increased to 0.626 at  $\text{Ca} = 5.22 \times 10^{-7}$ . In addition, the local saturation remained high across the sample. This increase in saturation with a decrease in  $\text{Ca}$  is consistent with other observations in 2D micromodels (Chen et al., 2017; Islam et al., 2014; Lenormand et al., 1988; Wang et al., 2013; Zhang et al., 2011).

#### 4.4. Number of fingers

We introduce the concept of the number of fingers to quantitatively discuss the change in structure of the IP in Fig. 4 during crossover between VF and CF. The ROI was separated into disk-shaped slab layers of 50-pixels (813  $\mu\text{m}$ ) thickness along the porous medium (Fig. 3e). For each slab layer of the separated IP, the number of fingers was counted (Fig. 8a-d). It worth noting that the definition of the number of fingers depends on the dimension of the packed bed used in an experiment; it quantitatively reflects the crossover of the fingering pattern.

The average number of fingers decreased with a decrease in  $\text{Ca}$  (Fig. 8e). For high  $\text{Ca}$  values ( $1.04 \times 10^{-4}$ ,  $5.22 \times 10^{-5}$ , and  $5.22 \times 10^{-6}$ ), the number of fingers was between four and ten, with an average of five to six, owing to the existence of streak-like structures for the VF (Fig. 8a). For lower  $\text{Ca}$  values, the average number of fingers decreased below three, reflecting the pattern of the CF, which developed in all directions (Chen et al., 2017; Islam et al., 2014; Lenormand et al., 1988; Wang et al., 2013; Zhang et al., 2011). In Fig. 8a-d, the structure of the IP is visualized and shows that a large space appeared in the 2D cross section (Fig. 8c), consisting of the trapped DF and glass beads. A magenta layer can be seen through the top yellow layer in Fig. 8d, but the IP was interconnected in a disk-shaped layer of 9-mm diameter and 813- $\mu\text{m}$  thickness. The ROI corresponded to the quarter domain from the inlet of the packed bed (height of 35 mm). Therefore, the horizontal connectivity of the IP was high in the ROI.

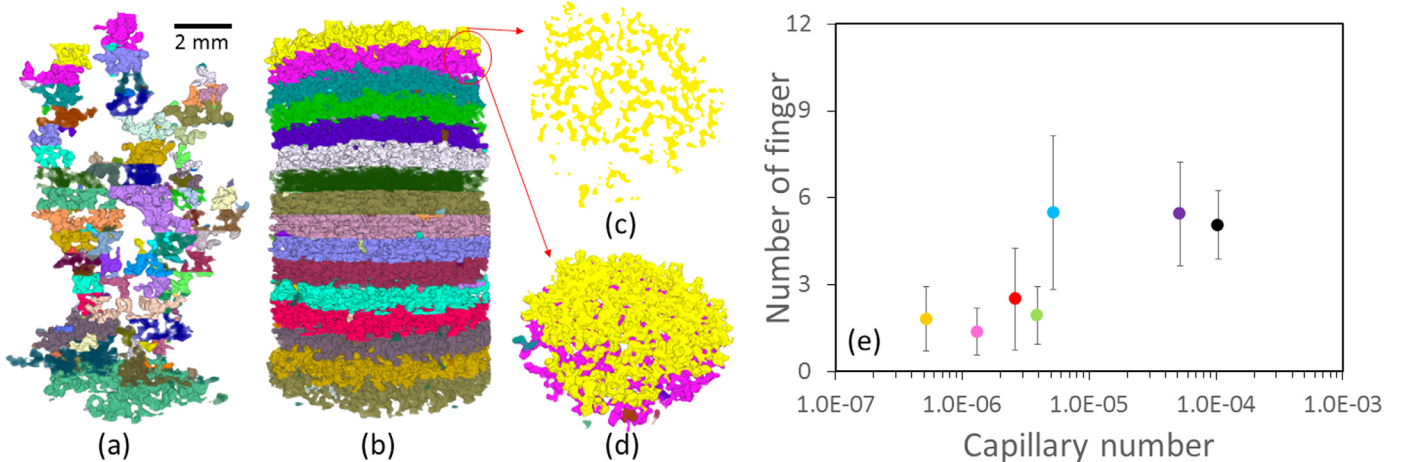


**Fig. 8.** Separated fingers labeled by color for  $Ca$  values of (a)  $1.04 \times 10^{-4}$  and (b)  $5.22 \times 10^{-7}$ . (c) 2D cross-sectional view at the top slice and (d) 3D structure of fingers in two top slabs for  $Ca = 5.22 \times 10^{-7}$ . (e) Average number of fingers versus  $Ca$  (error bars show standard deviation).

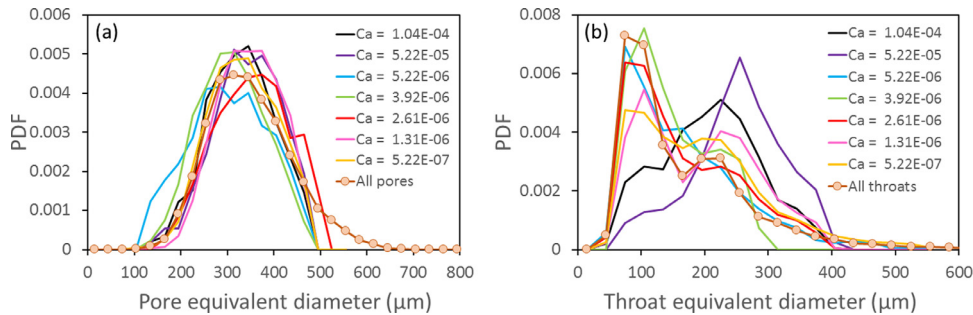


**Fig. 9.** Probability distribution function of invaded (a) pores and (b) throats by IP for all  $Ca$  values. Pore size distribution and throat size distribution of the porous medium are plotted as a tan line with circles.

#### 4.5. Pore and throat occupation of invading phase

The pore size distribution and throat size distribution of the porous medium are given in Fig. 9 as a tan line with circles as markers. The pore size distributes normally with a median pore diameter of  $206 \mu\text{m}$ , whereas the throat size shows a bimodal distribution with a median throat diameter of  $132 \mu\text{m}$  ( $105$  and  $195 \mu\text{m}$  at each peak). This bimodal distribution of throat corresponds to hexagonal formation of particles (a constriction generated between three contacting particles) and square formation of particles (a constriction generated between four contacting particles) in random sphere packing (Yang et al., 2006).

The probability distribution functions of the pores and throats occupied by the IP are given in Fig. 9a and b, respectively. The invaded pore size distributions show a normal distribution with similar average pore diameters and distributions for all  $Ca$  values, i.e., for both CF and VF. The invaded throat size clearly shifted from relatively large throats for VF to relatively small throats for CF. For high  $Ca$  values ( $1.04 \times 10^{-4}$  and  $5.22 \times 10^{-5}$ ), the IP tended to occupy larger throats and hardly invaded smaller throats. On the contrary, for low  $Ca$  values, the IP selectively penetrated the smaller throats. The shift in size associated with the crossover from VF to CF was observed in throat size distribution only because the entry capillary pressure was controlled by throats instead of pores. A throat is a constriction of the pore network; therefore, the throat becomes the position with the highest entry capillary pressure (Blunt, 2017). On the other hand, as the injection flow rate increases, viscous and capillary forces become more competitive, and the pressure in both IP and DP becomes non-uniform. As a consequence, the IP tends to invade the large throats because of low

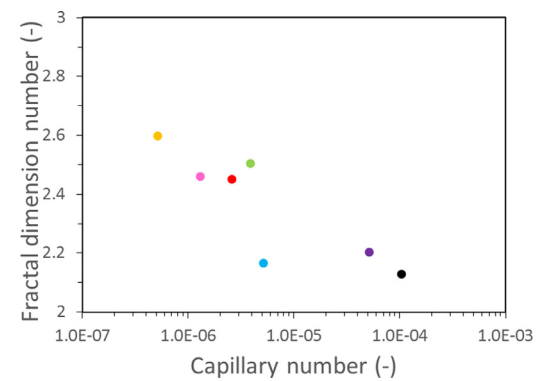


**Fig. 10.** Fractal dimension number of the IP for each injection condition.

viscous shear forces. It is worth noting that at  $Ca = 5.22 \times 10^{-6}$ , the structure of the IP (Fig. 5c) showed a streak-like pattern and the saturation was low (Fig. 7b), i.e., the throat occupation of the IP switched from VF to CF.

#### 4.6. Fractal dimension analysis

The fractal dimension of each of the displacement structures is given in Fig. 10. With a decrease in  $Ca$ , fractal dimension increases. High  $Ca$  values ( $1.04 \times 10^{-4}$ ,  $5.22 \times 10^{-5}$ , and  $5.22 \times 10^{-6}$ ), which correspond to VF, demonstrated the lowest fractal dimensions of about  $2.13$ – $2.21$ , whereas lowest  $Ca$  value ( $5.22 \times 10^{-7}$ ), which corresponds to CF, generated the highest fractal dimension of about  $2.60$ . For intermediate  $Ca$  values ( $3.92 \times 10^{-6}$ ,  $2.61 \times 10^{-6}$ ,

**Table 3**

Comparison of fractal dimensions with those of previous reports.

Citation	2D		3D	
	VF	CF	VF	CF
Present results	—	—	2.13–2.21	2.60
Chen et al. (2017)	1.64–1.72	1.69–1.79	—	—
Islam et al. (2014)	1.37–1.56	1.61–1.70	—	—
Toussaint et al. (2005)	1.53	1.83	—	—
Løvoll et al. (2004)	1.62	1.83	—	—
Holtzman and Juanes (2010)	1.64–1.71	1.77–1.82	—	—
Dias and Wilkinson (1986)	—	1.89	—	2.55
Wilkinson (1984)	—	—	—	2.50

and  $1.31 \times 10^{-6}$ ), which correspond to the crossover of VF–CF, the fractal dimension was between that of VF and CF (approximately 2.45–2.50). Nevertheless, this change in fractal dimension also corresponded to a change in displacement structure. For 3D objects, a lower fractal dimension indicates an object with lower ability to fill a volume, whereas higher fractal dimension indicates an object with greater ability to fill a volume (Mandelbrot, 1982), e.g., a 3D Hilbert (Romeu and Blanch, 2002.) curve and 3D Moore curve (Ali, 2009). This behavior also resembles the displacement structure of VF and CF. In VF, the streak-like structure resulted in less ability of the VF to fill the porous medium, whereas the ability of CF to invade in any direction led to a greater ability to fill more volume of the porous media. The VF–CF crossover fell between VF and CF. As a result, the fractal dimension of VF was the highest, that of CF the lowest, and that of the VF–CF crossover intermediate. To the best of our knowledge, the only available report on 3D displacement is the theoretical prediction of Wilkinson (1984) and Dias and Wilkinson (1986); this was for CF only. They predicted that the fractal dimension of CF in 3D porous media is about 2.50 and 2.55, respectively, which is similar to our results. Other reports of fractal dimension mainly relate to 2D micromodel systems (Chen et al., 2017; Holtzman and Juanes, 2010; Islam et al., 2014; Løvoll et al., 2004; Toussaint et al., 2005), with the fractal dimension of VF reported as being between 1.37 and 1.72 and of CF between 1.61 and 1.89. For comparison, all of the reported fractal dimensions for both 2D and 3D systems are given in Table 3.

## 5. Conclusions

We visualized the 3D fingering structure at breakthrough for a range of  $Ca$  values between  $5.22 \times 10^{-7}$  and  $1.04 \times 10^{-4}$  at the viscosity ratio of  $\log M = -2.203$  without the influence of buoyancy force. Imbibition experiments were performed with an immiscible fluid pair of water and oil with a packed bed of glass spheres with an average diameter of  $400\text{ }\mu\text{m}$ . Based on 3D CT images taken at a resolution of  $16.262\text{ }\mu\text{m}/\text{pixel}$ , the characteristics of the fingering pattern at the crossover from VF to CF were investigated quantitatively.

- Under a VF regime ( $Ca \geq 5.22 \times 10^{-6}$ ), the flow structure is streak-like owing to a forward-progressing pattern. Under a CF regime ( $Ca \leq 3.92 \times 10^{-6}$ ), the flow structure is more compact. The structure of the fingering pattern changed gradually from streak-like to more compact with a decrease in  $Ca$  from  $1.04 \times 10^{-4}$  to  $5.22 \times 10^{-7}$ . For CF ( $Ca = 5.22 \times 10^{-7}$ ), the size of trapped DP clusters distributes from the pore scale to several tens of pores and scaled with the exponent  $\tau \approx 1.1$ , which is consistent with previous observations (Iglauer and Wülling, 2016).
- The average saturation was low (0.096–0.110) under the VF regime, whereas it increased to 0.626 with the VF to CF crossover. We introduced the concept of the number of fingers to quantitatively discuss the change in IP structure.

3 The number of fingers is high for VF because the fingers extend selectively in the mean flow direction with streak-like structures. In the case of CF, the number of fingers is low (as compared with VF) because of an increase in the horizontal connectivity of the IP.

4 The packed bed of glass beads used in the present experiments shows a normal distribution of pore size, with an average pore diameter of  $206\text{ }\mu\text{m}$ , and a bimodal distribution of throat size, with a median throat diameter of  $132\text{ }\mu\text{m}$  ( $105$  and  $195\text{ }\mu\text{m}$  at each peak). The invaded pore size and invaded throat size distributions were also estimated for all  $Ca$  values. The invaded pore size distribution was similar for all  $Ca$  values but a clear shift in throat size was observed for the crossover from VF to CF. We clearly confirmed that imbibition is described by bond percolation, as expected.

5 The 3D structure of VF has a fractal number in the range 2.13–2.21. With a decrease in  $Ca$ , the fractal number increases up to 2.60, associated with the crossover from VF to CF.

## Declaration of Competing Interest

There is no conflict of interest to declare.

## Acknowledgments

This work was supported by JSPS KAKENHI with grant numbers 17H00790. Authors also greatly appreciate the support from the Indonesia Endowment Fund for Education (LPDP).

## Supplementary materials

Supplementary material associated with this article can be found, in the online version, at doi:[10.1016/j.ijmultiphaseflow.2019.103147](https://doi.org/10.1016/j.ijmultiphaseflow.2019.103147).

## References

- Ali, J.K., 2009. A new microstrip-fed printed slot antenna based on moore space-filling geometry. In: 2009 Loughborough Antennas & Propagation Conference. IEEE, pp. 449–452. doi:[10.1109/LAPC.2009.532551](https://doi.org/10.1109/LAPC.2009.532551).
- Armstrong, R.T., Evseev, N., Koroteev, D., Berg, S., 2015. Modeling the velocity field during Haines jumps in porous media. *Adv. Water Resour.* 77, 57–68. doi:[10.1016/j.advwatres.2015.01.008](https://doi.org/10.1016/j.advwatres.2015.01.008).
- Berg, S., Ott, H., Klapp, S.A., Schwing, A., Neiteler, R., Brussee, N., Makurat, A., Leu, L., Enzmann, F., Schwarz, J.-O., Kersten, M., Irvine, S., Stampaonni, M., 2013. Real-time 3D imaging of Haines jumps in porous media flow. *Proc. Natl. Acad. Sci.* 110, 3755–3759. doi:[10.1073/pnas.1221373110](https://doi.org/10.1073/pnas.1221373110).
- Blunt, M.J., 2017. Multiphase Flow in Permeable Media: A Pore Scale Perspective. Cambridge University Press, London doi:[10.1017/9781316145098](https://doi.org/10.1017/9781316145098).
- Bolte, S., Cordelieres, F.P., 2006. A guided tour into subcellular colocalisation analysis in light microscopy. *J. Microsc.* 224, 13–232. doi:[10.1111/j.1365-2818.2006.01706.x](https://doi.org/10.1111/j.1365-2818.2006.01706.x).
- Chen, Y.-F., Fang, S., Wu, D.-S., Hu, R., 2017. Visualizing and quantifying the crossover from capillary fingering to viscous fingering in a rough fracture. *Water Resour. Res.* 53, 7756–7772. doi:[10.1002/2017WR021051](https://doi.org/10.1002/2017WR021051).
- Danielsson, P.E., 1980. Euclidean distance mapping. *Comput. Graph. Image Process* 14, 227–248. doi:[10.1016/0146-664X\(80\)90054-4](https://doi.org/10.1016/0146-664X(80)90054-4).
- Dias, M.M., Wilkinson, D., 1986. Percolation with trapping. *J. Phys. A. Math. Gen.* 19, 3131–3146.
- Dullien, F.A.L., 1992. Porous Media: Fluid Transport and Pore Structure, second ed Elsevier, New York doi:[10.1016/C2009-0-26184-8](https://doi.org/10.1016/C2009-0-26184-8).
- Garing, C., Voltolini, M., Ajo-Franklin, J.B., Benson, S.M., 2017. Pore-scale evolution of trapped  $\text{CO}_2$  at early stages following imbibition using micro-CT imaging. *Energy Procedia* 114, 4872–4878. doi:[10.1016/j.egypro.2017.03.1628](https://doi.org/10.1016/j.egypro.2017.03.1628).
- Holtzman, R., Juanes, R., 2010. Crossover from fingering to fracturing in deformable disordered media. *Phys. Rev. E* 1–5. doi:[10.1103/PhysRevE.82.046305](https://doi.org/10.1103/PhysRevE.82.046305).
- Homzy, G.M., 1987. Viscous fingering in porous media. *Annu. Rev. Fluid Mech.* 19, 271–311. doi:[10.1146/annurev.fl.19.010187.001415](https://doi.org/10.1146/annurev.fl.19.010187.001415).
- Iglauer, S., Wülling, W., 2016. The scaling exponent of residual nonwetting phase cluster size distributions in porous media. *Geophys. Res. Lett.* 43 (11). doi:[10.1002/2016GL071298](https://doi.org/10.1002/2016GL071298), 253–11,260.
- Islam, A., Chevalier, S., Ben, I., Bernabe, Y., Juanes, R., Sassi, M., 2014. Characterization of the crossover from capillary invasion to viscous fingering to fracturing during drainage in a vertical 2D porous medium. *Int. J. Multiph. Flow* 58, 279–291. doi:[10.1016/j.ijmultiphaseflow.2013.10.002](https://doi.org/10.1016/j.ijmultiphaseflow.2013.10.002).

- Lashkarbolooki, M., Riazi, M., Hajibagheri, F., Ayatollahi, S., 2016a. Low salinity injection into asphaltene-carbonate oil reservoir, mechanistic study. *J. Mol. Liq.* 216, 377–386. doi:[10.1016/j.molliq.2016.01.051](https://doi.org/10.1016/j.molliq.2016.01.051).
- Lashkarbolooki, M., Vaezian, A., Hezave, A.Z., Ayatollahi, S., Riazi, M., 2016b. Experimental investigation of the influence of supercritical carbon dioxide and supercritical nitrogen injection on tertiary live-oil recovery. *J. Supercrit. Fluids* 117, 260–269. doi:[10.1016/j.supflu.2016.07.004](https://doi.org/10.1016/j.supflu.2016.07.004).
- Lenormand, R., Touboul, E., Zarcone, C., 1988. Numerical models and experiments on immiscible displacements in porous media. *J. Fluid Mech.* 189, 165. doi:[10.1017/S0022112088000953](https://doi.org/10.1017/S0022112088000953).
- Løvoll, G., Méheust, Y., Måløy, K.J., Aker, E., Schmittbuhl, J., 2005. Competition of gravity, capillary and viscous forces during drainage in a two-dimensional porous medium, a pore scale study. *Energy* 30, 861–872. doi:[10.1016/j.energy.2004.03.100](https://doi.org/10.1016/j.energy.2004.03.100).
- Løvoll, G., Méheust, Y., Toussaint, R., Schmittbuhl, J., Måløy, K.J., 2004. Growth activity during fingering in a porous Hele-Shaw cell. *Phys. Rev. E* 70, 026301.
- Mackay, D.M., Cherry, J.A., 1989. Groundwater contamination: pump-and-treat remediation. *Environ. Sci. Technol.* 23. doi:[10.1021/es00064a001](https://doi.org/10.1021/es00064a001).
- Mandelbrot, B.B., 1982. *The Fractal Geometry of Nature*. W.H. Freeman and Company, New York.
- Muharrik, M., Suekane, T., Patmonoaji, A., 2018. Effect of buoyancy on fingering growth activity in immiscible two-phase flow displacements. *J. Fluid Sci. Technol.* 13. doi:[10.1299/jfst.2018jfst0006](https://doi.org/10.1299/jfst.2018jfst0006).
- Nakanishi, Y., Hyodo, A., Wang, L., Suekane, T., 2016. Experimental study of 3D Rayleigh-Taylor convection between miscible fluids in a porous medium. *Adv. Water Resour.* 97, 224–232. doi:[10.1016/j.advwatres.2016.09.015](https://doi.org/10.1016/j.advwatres.2016.09.015).
- Ollion, J., Cochenne, J., Loll, F., Escudé, C., Boudier, T., 2013. TANGO: a generic tool for high-throughput 3D image analysis for studying nuclear organization. *Bioinformatics* 29, 1840–1841. doi:[10.1093/bioinformatics/btt276](https://doi.org/10.1093/bioinformatics/btt276).
- Patmonoaji, A., Suekane, T., 2017. Investigation of CO<sub>2</sub> dissolution via mass transfer inside a porous medium. *Adv. Water Resour.* 110, 97–106. doi:[10.1016/j.advwatres.2017.10.008](https://doi.org/10.1016/j.advwatres.2017.10.008).
- Patmonoaji, A., Tsuji, K., Muharrik, M., Suekane, T., 2018. Micro-tomographic analyses of specific interfacial area inside unconsolidated porous media with differing particle characteristics from microscopic to macroscopic scale. *J. Colloid Interface Sci.* 532, 614–621. doi:[10.1016/j.jcis.2018.08.023](https://doi.org/10.1016/j.jcis.2018.08.023).
- Romeu, J., Blanch, S., 2002. A three dimensional hilbert antenna. In: *IEEE Antennas and Propagation Society International Symposium*, pp. 550–553.
- Roozbahani, M.M., Huat, B.B.K., Asadi, A., 2012. Effect of rectangular container's sides on porosity for equal-sized sphere packing. *Powder Technol.* 224, 46–50. doi:[10.1016/j.powtec.2012.02.018](https://doi.org/10.1016/j.powtec.2012.02.018).
- Saffman, P.G., 1986. Viscous fingering in Hele-Shaw cells. *J. Fluid Mech.* 173, 73–94. doi:[10.1017/S0022112086001088](https://doi.org/10.1017/S0022112086001088).
- Suekane, T., Okada, K., 2013. Gas injection in a water saturated porous medium: effect of capillarity, buoyancy, and viscosity ratio. *Energy Procedia* 37, 5545–5552. doi:[10.1016/j.egypro.2013.06.475](https://doi.org/10.1016/j.egypro.2013.06.475).
- Suekane, T., Saito, Y., Jiang, L., 2015. Non-wetting phase saturation after drainage from the wetting-phase-filled porous medium. *J. Fluid Sci. Technol.* 10. doi:[10.1299/jfst.2015jfst0014](https://doi.org/10.1299/jfst.2015jfst0014), JFST0014–JFST0014.
- Toussaint, R., Løvoll, G., Meheust, Y., Maløy, K.J., Schmittbuhl, J., 2005. Influence of pore-scale disorder on viscous fingering during drainage. *Europhys. Lett.* 71, 583–589. doi:[10.1209/epl/i2005-10136-9](https://doi.org/10.1209/epl/i2005-10136-9).
- Tsuji, T., Jiang, F., Christensen, K.T., 2016. Characterization of immiscible fluid displacement processes with various capillary numbers and viscosity ratios in 3D natural sandstone. *Adv. Water Resour.* 95, 3–15. doi:[10.1016/j.advwatres.2016.03.005](https://doi.org/10.1016/j.advwatres.2016.03.005).
- Wang, L., Nakanishi, Y., Hyodo, A., Suekane, T., 2016. Three-dimensional structure of natural convection in a porous medium: effect of dispersion on finger structure. *Int. J. Greenh. Gas Control* 53, 274–283. doi:[10.1016/j.ijggc.2016.08.018](https://doi.org/10.1016/j.ijggc.2016.08.018).
- Wang, Y., Zhang, C., Wei, N., Oostrom, M., Wietsma, T.W., Li, X., Bonneville, A., 2013. Experimental study of crossover from capillary to viscous fingering for supercritical CO<sub>2</sub>-water displacement in a homogeneous pore network. *Environ. Sci. Technol.* 47, 212–218. doi:[10.1021/es3014503](https://doi.org/10.1021/es3014503).
- Wilkinson, D., 1984. Percolation model of immiscible displacement in the presence of buoyancy forces. *Phys. Rev. A* 30, 520–531. doi:[10.1103/PhysRevA.30.520](https://doi.org/10.1103/PhysRevA.30.520).
- Wilkinson, D., Willemse, J.F., 1983. Invasion percolation: a new form of percolation theory. *J. Phys. A. Math. Gen.* 16, 3365–3376. doi:[10.1088/0305-4470/16/14/028](https://doi.org/10.1088/0305-4470/16/14/028).
- Yang, R.Y., Zou, R.P., Yu, A.B., Choi, S.K., 2006. Pore structure of the packing of fine particles. *J. Colloid Interface Sci.* 299, 719–725. doi:[10.1016/j.jcis.2006.02.041](https://doi.org/10.1016/j.jcis.2006.02.041).
- Zacharoudiou, I., Boek, E.S., Crawshaw, J., 2018. The impact of drainage displacement patterns and Haines jumps on CO<sub>2</sub> storage efficiency. *Sci. Rep.* 8, 1–13. doi:[10.1038/s41598-018-33502-y](https://doi.org/10.1038/s41598-018-33502-y).
- Zhang, C., Oostrom, M., Wietsma, T.W., Grate, J.W., Warner, M.G., 2011. Influence of viscous and capillary forces on immiscible fluid displacement: pore-scale experimental study in a water-wet micromodel demonstrating viscous and capillary fingering. *Energy Fuels* 25, 3493–3505. doi:[10.1021/ef101732k](https://doi.org/10.1021/ef101732k).